Interbasin Transport of the Meridional Overturning Circulation

C. S. JONES AND PAOLA CESSI

Scripps Institution of Oceanography, University of California, San Diego, La Jolla, California

(Manuscript received 16 October 2015, in final form 12 January 2016)

ABSTRACT

The meridional overturning circulation (MOC) is studied in an idealized domain with two basins connected by a circumpolar channel in the southernmost region. Flow is forced at the surface by longitude-independent wind stress, freshwater flux, and fast temperature relaxation to prescribed profiles. The only longitudinal asymmetry is that one basin is twice as wide as the other. Two states, a preferred one with sinking in the narrow basin and an asymmetrically forced one with sinking in the wide basin, are compared. In both cases, sinking is compensated by upwelling everywhere else, including the passive basin. Despite the greater area of the wide basin, the residual overturning transport is the same regardless of the location of sinking. The two basins exchange flow at their southern edge by a geostrophic transport balanced by the difference in the depth of isopycnals at the eastern boundaries of each basin. Gnanadesikan's model for the upper branch of the MOC is extended to include two basins connected by a reentrant channel and is used to illustrate the basic properties of the flow: the layer containing the surface and intermediate water is shallower in the active basin than in the passive basin, and this difference geostrophically balances an exchange flow from the passive to the active basin. The exchange flow is larger when sinking occurs in the narrow basin. A visualization of the horizontal structure of the upper branch of the MOC shows that both the gyres and the meridional flow are important in determining the flow field.

1. Introduction

In the current climate system, deep water is formed in the North Atlantic, but not in the North Pacific, resulting in a global meridional overturning circulation (MOC) that transports heat northward in the Atlantic and contributes to a more marked southward heat flux in the South Indo-Pacific. The MOC is a global cell, driven by the wind-induced upwelling in the circumpolar region (Toggweiler and Samuels 1993; Wolfe and Cessi 2010), as well as by diffusive upwelling at the interface between the deep and abyssal waters (Stommel and Arons 1959; Munk 1966), dominated by the contribution in the Indo-Pacific sector. The upwelling in the circumpolar portion of the domain and in the passive basin (the Pacific) is balanced by downwelling near the northern end of the active basin (the Atlantic). This global circulation implies a transfer of intermediate water from the passive into the active basin (with a transfer of deep water in the opposite direction). This transfer occurs in the circumpolar region, as detailed in Talley (2013) (there is also a small exchange through the Bering Strait, which we neglect henceforth). The transfer of water between the basins is geostrophically balanced at the southern boundary of each semienclosed basin, requiring a difference in the depth of the isopycnals separating the intermediate and deep waters at the eastern boundary of each basin. Specifically, these isopycnals are deeper in the South Pacific than in the South Atlantic in the present-day MOC, as noted by Reid (1961). More recent observations from the *World Ocean Atlas* (Locarnini et al. 2006; Antonov et al. 2006) confirm that isopycnals near 1000 m depth are shallower in the Atlantic than in the Indo-Pacific (see Fig. 1). The strength of the interbasin flow is set by the amount of Ekman transport and the upwelling into the intermediate waters of the Indo-Pacific. The interbasin transfer is only one component of the total transport that forms the upper branch of the MOC: in addition to the interbasin flow, the MOC, or more precisely the residual overturning circulation (ROC), must carry all of the Ekman transport that occurs along the northern boundary of the Antarctic Circumpolar Current (ACC) region, minus

Corresponding author address: C. S. Jones, Scripps Institution of Oceanography, University of California, San Diego, 9500 Gilman Dr., M/C 0213, La Jolla, CA 92039-0213.
E-mail: csjones@ucsd.edu

DOI: 10.1175/JPO-D-15-0197.1

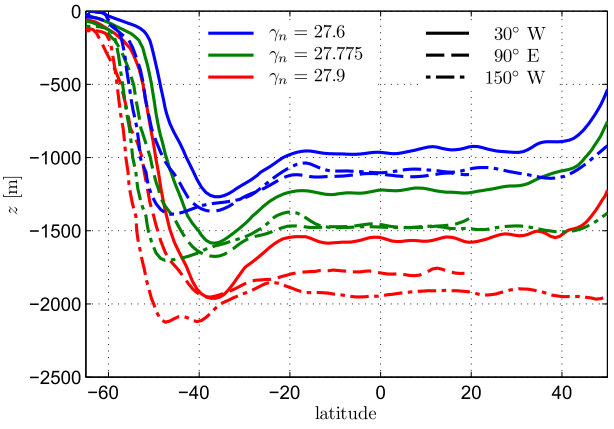

FIG. 1. Depth of three middepth neutral density γ_n surfaces as a function of latitude at three longitudes corresponding to the Atlantic (30°W), Indian (90°E), and Pacific (150°W) Oceans. Lines that are the same color represent the same value of γ_n, whereas lines that are the same style represent the same longitude. From Wolfe and Cessi (2010).

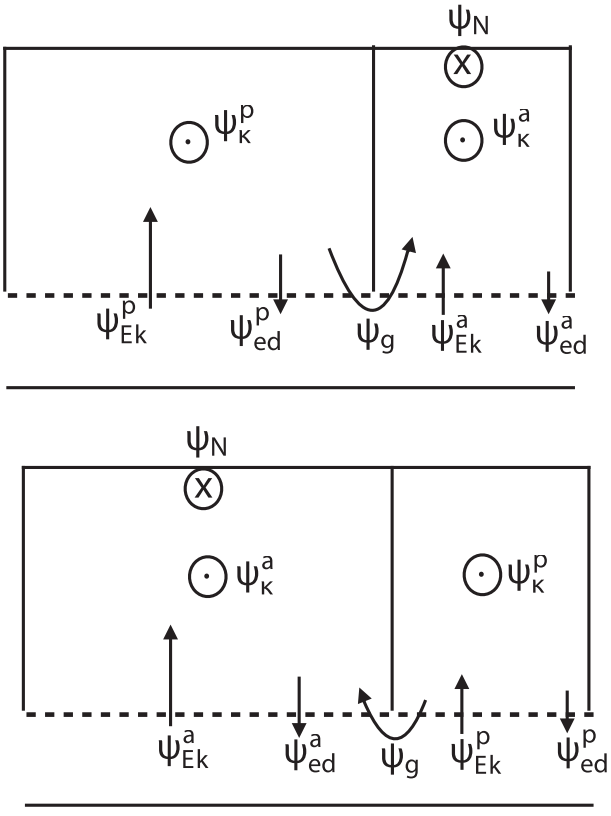

FIG. 2. Schematic of the two-basin box model, showing the transport budget above the isopycnal bounding the upper branch of the ROC for sinking in the (top) narrow basin and (bottom) wide basin. The ⊗ denotes sinking (transport from the upper layer into the lower layer) and the ⊙ denotes upwelling (transport from the lower layer into the upper layer). Variable ψ_N represents northern sinking in the active basin, ψ_κ represents diapycnal upwelling, ψ_{Ek} represents the Ekman transport at the northern edge of the channel region, ψ_{ed} represents the eddy fluxes at the northern edge of the channel region, and ψ_g represents a geostrophic exchange transport, which flows out of the passive and into the active basin in the upper layer.

the eddy flux of buoyancy at this boundary, as well as the diapycnal upwelling in the Atlantic.

The mechanism for size-dependent interbasin transport is illustrated here by considering a generalization of the model by Gnanadesikan (1999) to two basins connected by a circumpolar region. A geostrophically balanced interbasin flow ψ_g, which transfers water from the passive basin to the active basin, is necessary to satisfy the buoyancy budget (as shown in Fig. 2). The depth of the intermediate water layer must be deeper in the passive basin than in the active basin in order to geostrophically balance the interbasin flow. The transfer from the passive to the active basin is fed by diffusive upwelling and Ekman transport into the passive basin, and therefore the transfer is larger when the passive basin is wider. This simple model does not capture the richness of the horizontal and vertical structure of the ROC velocity field, spanning both the active and the passive basins, which we diagnose from three-dimensional numerical integrations.

These three-dimensional integrations follow the approach of Hughes and Weaver (1994) and Marotzke and Willebrand (1991), that is, we use an ocean-only model with drastically simplified geometry and forcing. There is a two-basin geometry in which the latitudinal extent of the two basins is the same. In this, we differ from the basic configuration of Hughes and Weaver (1994), who specified that the Atlantic-like basin extends farther north than the Pacific-like basin. The purpose of our configuration is to determine the consequences of differences in the longitudinal extent of the Atlantic- and Pacific-like basins. We confine our analysis to the weakly diffusive regime, where the ROC has a substantial adiabatic component associated with the wind-driven upwelling in the circumpolar portion of the domain (Toggweiler and Samuels 1993; Wolfe and Cessi 2010).

The partition of the MOC between the Atlantic and Indo-Pacific sector in an idealized domain was also studied by Stocker and Wright (1991), using a zonally averaged model, with a parameterization relating the east–west pressure gradient to the north–south one. They found that under zonally symmetric forcing, the system settles into a state with two separate overturning cells with sinking at the northern edge of both the North Atlantic and the North Pacific and little transfer between the two basins. Some ocean-only studies (Seidov and Haupt 2005) find that it is necessary to impose an asymmetry in the surface salinity or freshwater flux to achieve a conveyor-like global overturning circulation,

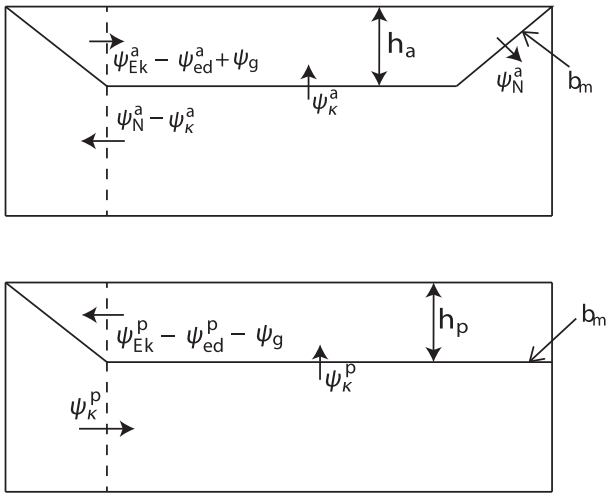

FIG. 3. Schematic of the two-basin box model, showing the transport budget above the isopycnal bounding the upper branch of the ROC for the (top) active basin and (bottom) passive basin. Variable b_m is the isopycnal that divides the upper layer and the lower layer and $h_{a,p}$ denotes the height of the upper layer. The other symbols are defined in Fig. 2.

while others find that multiple states exist depending on the initial conditions (Huisman et al. 2009). Nilsson et al. (2013) find that in a coupled model, conveyor-like states exist (in which sinking occurs in only one basin) as well as a northern-sinking state (in which sinking occurs in the north of both basins). In the quasi-adiabatic regime, we find that under longitudinally symmetric forcing, stable sinking is obtained only at the northern end of the narrow basin, a state that maximizes the interbasin exchange of the ROC. No other states exist for symmetric forcing. To achieve sinking in the wide basin, the surface forcing is modified to decrease precipitation over the wide basin. The interbasin transport ψ_g in each of these states compares well to the predictions of the two-basin zonally averaged model.

Section 2 proposes an idealized zonally average model adapted from Gnanadesikan (1999). The numerical model setup and some of the diagnostics are described in section 3. Section 4 describes the numerical model states, and section 5 illustrates the horizontal structure of the flow in the ROC. A summary and concluding remarks are given in section 6.

2. A minimal model of two basins exchanging transport

Here, we consider an extension of the Gnanadesikan (1999) model of the ROC to two basins coupled by a circumpolar connection, as sketched in Figs. 2 and 3. This model is very similar to that developed in Allison (2009); however, in that model the lengths of the boundaries are different. It crudely captures the circulation in the upper branch of the ROC; the upper branch is defined to be the layer above the isopycnal b_m, which divides the intermediate water from the deep water. In the context of this model, the layer above b_m is referred to as the upper layer and the layer below b_m is referred to as the lower layer. Thickness is transferred between the layers through northern sinking, diapycnal upwelling, and Ekman and eddy fluxes.

From Fig. 2, we can see that the buoyancy budget of the upper layer for the semienclosed portions of each basin is given by

$$\psi^a_{\rm Ek} - \psi^a_{\rm ed} + \psi^a_\kappa + \psi_g = \psi_N, \quad \text{and} \tag{1}$$

$$\psi^p_{\rm Ek} - \psi^p_{\rm ed} + \psi^p_\kappa - \psi_g = 0, \tag{2}$$

where $\psi_{\rm Ek}$ denotes the Ekman transport entering the basins from the circumpolar region, $\psi_{\rm ed}$ is the transport of buoyancy by eddy fluxes southward into the channel region [modeled here using the Gent–McWilliams (Gent and McWilliams 1990, hereinafter GM) parameterization; see section 3], ψ_κ is a diapycnal exchange of buoyancy across the isopycnal b_m, ψ_g is the geostrophically balanced exchange that results from the difference in zonal flow in the two sectors of the circumpolar domain, and ψ_N is the transport due to sinking at the northern edge of the domain. We choose to explore the special case in which sinking ψ_N only occurs in one basin or the other. The superscripts "a" and "p" refer to the active and passive basins, respectively.

In this model the depth of the isopycnal b_m is given by h_a in the active basin and h_p in the passive basin, as shown in Fig. 3. Following Gnanadesikan (1999), we can substitute standard expressions for Ekman, eddy, diapycnal, and geostrophic transports into (1) and (2) to arrive at the system

$$\underbrace{-\frac{\tau_s L_a}{\rho_0 f_s}}_{\psi^a_{\rm Ek}} \underbrace{-\frac{\kappa_{\rm GM} h_a L_a}{L_c}}_{\psi^a_{\rm ed}} + \underbrace{\frac{\kappa A_a}{h_a}}_{\psi^a_\kappa} \underbrace{-\frac{g'(h_p^2 - h_a^2)}{2 f_s}}_{\psi_g} = \underbrace{g'\frac{h_a^2}{2 f_n}}_{\psi_N}, \tag{3}$$

and

$$\underbrace{-\frac{\tau_s L_p}{\rho_0 f_s}}_{\psi^p_{\rm Ek}} \underbrace{-\frac{\kappa_{\rm GM} h_p L_p}{L_c}}_{\psi^a_{\rm ed}} + \underbrace{\frac{\kappa A_p}{h_p}}_{\psi^p_\kappa} + \underbrace{\frac{g'(h_p^2 - h_a^2)}{2 f_s}}_{\psi_g} = 0. \tag{4}$$

We have denoted the widths of the basins with $L_{a,p}$, τ_s is the wind stress that drives Ekman transport out of the reentrant channel, f_s is the Coriolis parameter at the southern boundary of the semienclosed portion of the domain, f_n is the Coriolis parameter at 57.5°N, L_C is the meridional extent of the circumpolar channel, $\kappa_{\rm GM}$ is the coefficient

TABLE 1. The external parameters for the simplified two-basin transport budget, as deduced from the numerical simulations.

Parameter	Value	Notes
κ_{GM}	$500\,m^2\,s^{-1}$	Value used in the numerical model
L_p	10 000 km	Width of the wide basin at the channel edge
L_a	5000 km	Width of the narrow basin at the channel edge
L_c	2000 km	North–south extent of the channel
A_a	$4 \times 10^{13}\,m^2$	Area of the narrow basin north of the channel and south of the equator
A_p	$8 \times 10^{13}\,m^2$	Area of the wide basin north of the channel and south of the equator
ρ_0	$1000\,kg\,m^{-3}$	The average density
$f_n = -f_s$	$1.2 \times 10^{-4}\,s^{-1}$	$\|f\|$ at 57.5°S, the northern edge of the channel
κ	$2 \times 10^{-5}\,m^2\,s^{-1}$	Value used in the numerical model
τ	0.1	Average wind stress along the northernmost barotropic contour in the reentrant channel
g'	$0.004\,m\,s^{-2}$	Approximate range of buoyancy shared between the channel and the northern end of the active basin

of GM eddy fluxes parameterization, κ is the interior diapycnal diffusivity, $A_{a,p}$ represents the area of the semienclosed basins, g' is the range of surface buoyancies shared by the sinking and circumpolar regions. Wind stress τ_s is the average along the northernmost periodic barotropic streamline in the circumpolar region. This is the most appropriate definition of the northern edge of the reentrant channel (Marshall et al. 2016). The values of the prescribed parameters are given in Table 1.

The novel term here is the geostrophic transport ψ_g exchanged between the two basins, proportional to the difference between the squared heights of the upper layer at the eastern boundaries of each basin. At the southern edge of the semienclosed region, the height of the upper layer at the eastern boundary of one basin must be equal to the height of the upper layer at the western boundary of the other basin, in order to ensure no normal flow into the southern edge of the continent. In the system (3) and (4), we identify the characteristic depth of the isopycnal b_m in each basin with its depth at the eastern boundary. Therefore, the geostrophic transport ψ_g into the upper layer of the active basin is proportional to the squared height of the upper layer at the eastern edge of the active basin h_a minus the squared height of the upper layer at the eastern edge of the passive basin h_p. The geostrophic transport into the passive basin is $-\psi_g$, because the two heights are switched.

The system (3) and (4) can be solved for $h_{a,p}$, given the external parameters for geometry, forcing, and diffusion. With the formulation (3) and (4), sinking in the narrow basin and sinking in the wide basin can be studied by simply exchanging the values of L_a, A_a with L_p, A_p.

Taking the sum of (3) and (4), ψ_g cancels out and we find

$$\psi^a_{\rm Ek} - \psi^a_{\rm ed} + \psi^p_{\rm Ek} - \psi^a_{\rm ed} + \psi^a_\kappa + \psi^p_\kappa = \psi_N. \qquad (5)$$

Assuming that the difference in isopycnal heights is small compared with their total depth, that is, $h_p = h_a + \epsilon$, with $\epsilon \ll h_a$, it is clear that the total amount of sinking ψ_N is, to leading order in ϵ, the same as that obtained in a single basin whose width is $L_a + L_p$ and whose area is $A_a + A_p$. In the same limit, the difference in isopycnal heights, $\epsilon \equiv h_p - h_a$, is given by

$$\epsilon\left[\frac{\kappa_{GM}}{L_c} + \frac{\kappa L_c}{h_a^2} + \frac{g' h_a (L_a + L_p)}{L_a L_p |f_s|}\right] = g' \frac{h_a^2}{2 f_n L_a}. \qquad (6)$$

This shows that $\epsilon > 0$, that is, the isopycnal b_m is always deeper in the passive basin, because the term inside the square bracket on the left-hand side (lhs) of (6) is always positive, as is the right-hand side (rhs). In addition, (6) shows that ϵ and ψ_g are larger when sinking occurs in the narrow basin: if we exchange L_a with L_p, the term inside the square bracket on the lhs remains the same, while the rhs decreases. The resulting depths, $h_{a,p}$, and associated transport for sinking in the narrow or wide basin are given in Table 2 for the parameters used listed in Table 1. We choose the cases $L_a = 2L_p$ and $L_p = 2L_a$. However, it is of interest to note that if $A_a \to 0$, $h_a \sim h_p/\sqrt{2}$, and when $A_p \to 0$, $h_a \sim h_p$.

The essential point is that sinking in the narrow basin leads to a larger interbasin flow, and a larger residual circulation per unit width, than sinking in the wide basin.

TABLE 2. Results of the simplified two-basin model, based on (3) and (4), compared to the numerical MITgcm simulations.

	Sinking in the narrow basin	MITgcm in narrow sinking	Sinking in the wide basin	MITgcm wide sinking
ψ_N	11.3 Sv	11.8 Sv	11.9 Sv	11.9 Sv
ψ_g	7.2 Sv	8.2 Sv	3.8 Sv	3.1 Sv
$\psi^p_{\rm Ek}$	8.3 Sv		4.2 Sv	
$\psi^a_{\rm Ek}$	4.2 Sv		8.3 Sv	
$\psi^p_{\rm ed}$	2.6 Sv		1.2 Sv	
$\psi^a_{\rm ed}$	1.0 Sv		2.1 Sv	
ψ^p_κ	1.5 Sv		0.8 Sv	
ψ^a_κ	1.0 Sv		1.8 Sv	
h_a	824 m	841 m	845 m	821 m
h_p	1055 m	1016 m	970 m	882 m

The reason for this asymmetry is simple: if sinking occurs in the narrow basin, then all of the residual flow entering the upper layer in the wide basin through Ekman transport (minus the eddy contribution) and diapycnal mixing must enter the narrow basin to sink, adding to the Ekman transport directly entering the active basin. Regardless of the location of sinking, the residual transport is given by the sum of the Ekman transport at the northern edge of the channel (minus the eddy transport), and the diapycnal upwelling throughout both basins. Thus, the transport per unit width is larger when sinking occurs in the narrow basin.

In the following section the predictions of this simple box model are examined with a three-dimensional primitive equation GCM.

3. Model and diagnostics

The numerical model employed is the Massachusetts Institute of Technology general circulation model (MITgcm; Marshall et al. 1997a,b), which integrates the hydrostatic, Boussinesq primitive equations. The domain is a spherical sector spanning 140° in latitude and 210° in longitude with a 1° horizontal resolution. The geometrical configuration comprises two idealized basins, one twice as wide as the other, joined by a reentrant channel of latitudinal width 17.5° at the southern edge of the domain as shown in Fig. 4. The bottom is flat and 4000 m deep, except for a sill in the periodic channel, 1 grid point wide and 1333 m high, located immediately south of the narrow basin's western boundary.[1] There are 32 unequally spaced levels in the vertical, ranging from a minimum spacing of 13.6 m at the top to a maximum of 286 m at the bottom.

The equation of state is linear, so that the buoyancy is described by

$$b = g[\alpha_T T - \beta_S (S - S_{\text{ref}})], \tag{7}$$

where $\alpha_T = 2 \times 10^{-4}\,^{\circ}\text{C}^{-1}$, $\beta_S = 7.4 \times 10^{-4}$, and $S_{\text{ref}} = 35$. Salinity is given on the practical salinity scale and is therefore described without units.

The surface forcings are steady and zonally uniform: the expressions for the wind stress τ, freshwater flux F, and distribution to which the surface temperature is relaxed T^*, are given by

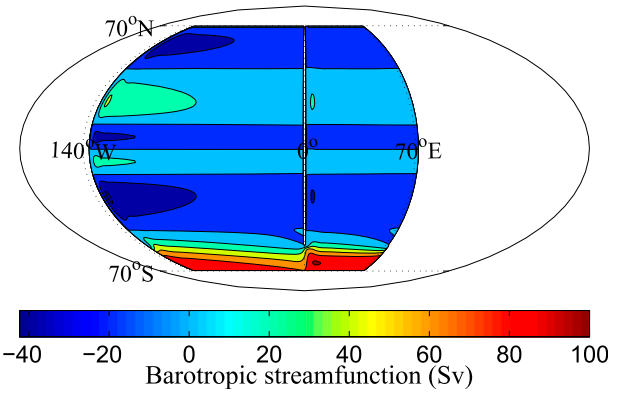

FIG. 4. Barotropic streamfunction and geometry of the domain used in the computations. The domain is 210° periodic and 4000 m deep.

$$\tau = \tau_{\text{Max}}[-\cos(3\pi\theta/140) + 1e^{-\theta^2/2\sigma^2}], \tag{8}$$

$$F = F_{s0}[\cos(7\pi\theta/8\Theta) - 2e^{-(\theta/\Theta)^2/(2\sigma_F^2)}] - F_0, \quad \text{and} \tag{9}$$

$$T^* = T_{\text{eq}}[\cos(\pi\theta/140)^2 + 0.1e^{-(\theta/2\Theta - 1)^2}]. \tag{10}$$

We adopt the following notation: θ is latitude in degrees, $\tau_{\text{Max}} = 0.1$ Pa, $\sigma = 10°$, $F_{s0} = 2 \times 10^{-8}\,\text{m s}^{-1}$, $\sigma_F = 0.128$, $\Theta = 60°$, and $T_{\text{eq}} = 25°$C. The relaxation time scale for the surface temperature is 10 days. The constant F_0 is defined such that the area-averaged freshwater flux $\langle F \rangle = 0$. The freshwater flux is then turned into a virtual salt flux by multiplying F by -35. The distributions of τ, F, and T^* as a function of latitude are shown in Fig. 5.

Momentum is dissipated via Laplacian viscosity with horizontal and vertical coefficients $\nu_h = 4 \times 10^4\,\text{m}^2\,\text{s}^{-1}$ and $\nu_v = 1 \times 10^4\,\text{m}^2\,\text{s}^{-1}$, respectively; we employ no-slip sidewalls and a free-slip bottom augmented by a linear bottom drag with coefficient $r = 3.5 \times 10^{-6}\,\text{s}^{-1}$ applied over the bottom grid cell. Because of the coarse model resolution, baroclinic eddies are parameterized using the advective form of GM and Redi (1982) isopycnal mixing with equal mixing coefficients $K_{\text{GM}} = 500\,\text{m}^2\,\text{s}^{-1}$. GM is implemented using the boundary value problem scheme of Ferrari et al. (2010) with vertical mode number $m = 2$ and minimum wavespeed $c_{\text{min}} = 0.1\,\text{m s}^{-1}$. The Redi tensor is tapered exponentially to horizontal diffusion in regions of weak stratification using the method of Danabasoglu and McWilliams (1995).

Tracers are advected using the second-order-moments (SOM) scheme of Prather (1986) and diffused using a vertical diffusivity κ, which is surface intensified to mimic an idealized mixed layer such that

$$\kappa = \kappa_v + \kappa_m[1 + \tanh(z + d)/d], \tag{11}$$

where $\kappa_v = 2 \times 10^{-5}\,\text{m}^2\,\text{s}^{-1}$ is the diffusivity in the deep ocean, $\kappa_m = 10^{-2}\,\text{m}^2\,\text{s}^{-1}$ is the diffusivity at the surface,

[1] The experiments described here have been repeated in a domain with two sills, one at the southern end of each boundary. The qualitative properties of these experiments are the same, confirming that the sill does not cause the preference for narrow basin sinking.

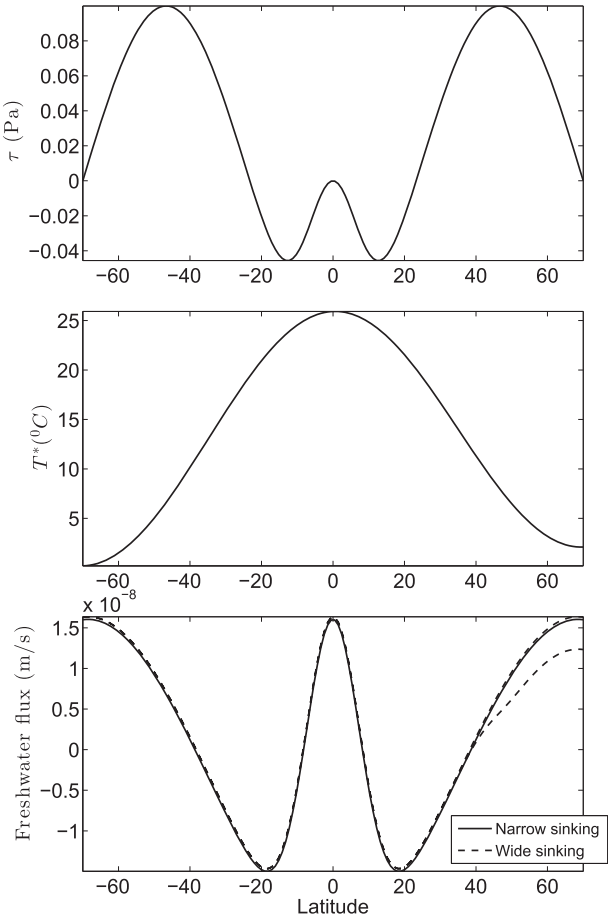

FIG. 5. Forcing fields as a function of latitude: (top) wind stress, (middle) relaxation temperature, and (bottom) freshwater flux. The dashed lines show the freshwater flux applied to induce a sinking in the wide basin. Where these lines split, the upper dashed line is applied to the narrow basin and the lower is applied to the wide basin.

and $d = 20\,\mathrm{m}$ is the characteristic depth of the mixed layer.

Residual overturning streamfunction

The overturning circulation is quantified using the zonally integrated residual overturning streamfunction (cf. Wolfe and Cessi 2015):

$$\psi(y,\tilde{b}) \equiv \frac{1}{T}\int_0^T \int_0^{L_x} \int_{-H}^{0} v^{\dagger}\mathcal{H}[b(x,y,z,t)-\tilde{b}]\,dz\,dx\,dt, \tag{12}$$

where $T = 100$ years, $v^{\dagger} = v + v_{\mathrm{GM}}$ is the total meridional velocity (the sum of the resolved velocity v and the eddy velocity from the GM parameterization v_{GM}), and $\mathcal{H}$ is the Heaviside step function. The variable ψ is the zonally integrated transport of water above the isopycnal $b(x, y, z, t) = \tilde{b}$. The "vertical" coordinate $\tilde{b}$ is buoyancy; the tilde distinguishes the coordinate buoyancy from the buoyancy field.

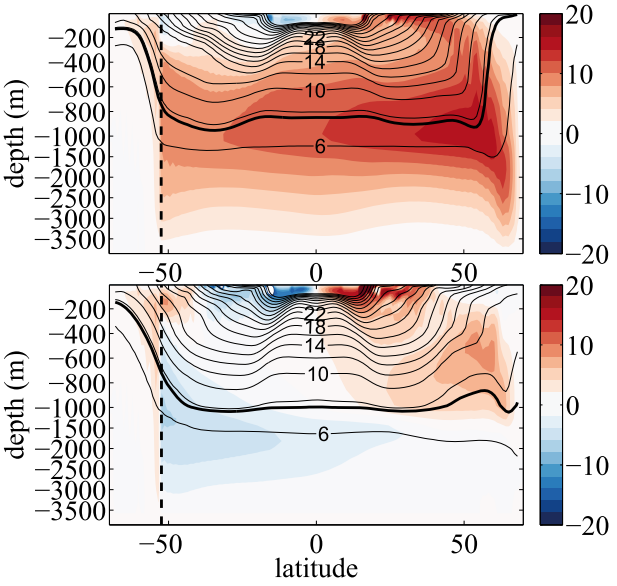

FIG. 6. Residual overturning streamfunction in Sverdrups (color contours, interval 2 Sv) and $b^{\sharp} \times 10^3\,\mathrm{m\,s^{-2}}$, the buoyancy of the surface whose average depth is z (black contours) in the (top) narrow basin and (bottom) wide basin. Sinking is in the narrow basin. In both plots, the reentrant channel region (left of the thick black dotted line) shows the total streamfunction over all longitudes. The thick black contour denotes the isopycnal $b_m = 0.0076\,\mathrm{m\,s^{-2}}$, which bounds the upper branch of the ROC.

For presentation purposes, ψ is remapped into height coordinates using the mean isopycnal height

$$\zeta(y,\tilde{b}) \equiv -\frac{1}{T}\int_0^T \frac{1}{L_x}\int_0^{L_x} \int_{-H}^{0} \mathcal{H}[b(x,y,z,t)-\tilde{b}]\,dz\,dx\,dt. \tag{13}$$

In height coordinates, ψ advects a modified buoyancy $b^{\sharp}(y, z)$ that satisfies $\zeta[y, b^{\sharp}(y, z)] = z$; that is, ψ is constant on $b^{\sharp}$ contours for purely adiabatic flow.

Because of zonal buoyancy gradients, the remapping distorts the vertical extent of the mixed layer. Buoyancies higher than $40 \times 10^{-3}\,\mathrm{m\,s^{-2}}$ are not plotted because the contours are too close together.

4. Pacific and Atlantic overturnings

With the forcing in Fig. 5, the model settles into a narrow-sinking state where sinking occurs at the northern end of the narrow basin. The resulting overturning circulation is shown in Fig. 6 (colors and gray contours), together with $b^{\sharp}$ (black contours). The maximum ψ is 15 Sverdrups (Sv; $1\,\mathrm{Sv} \equiv 10^6\,\mathrm{m^3\,s^{-1}}$) near the northern end of the narrow basin and the interhemispheric

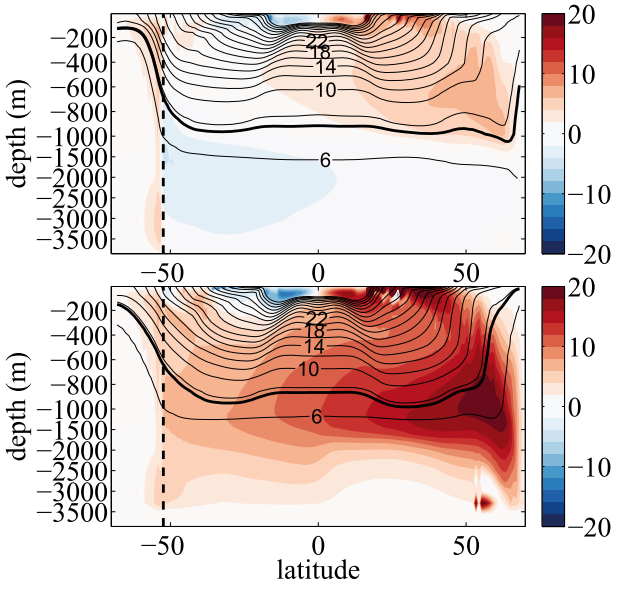

FIG. 7. As in Fig. 6, but sinking is in the wide basin.

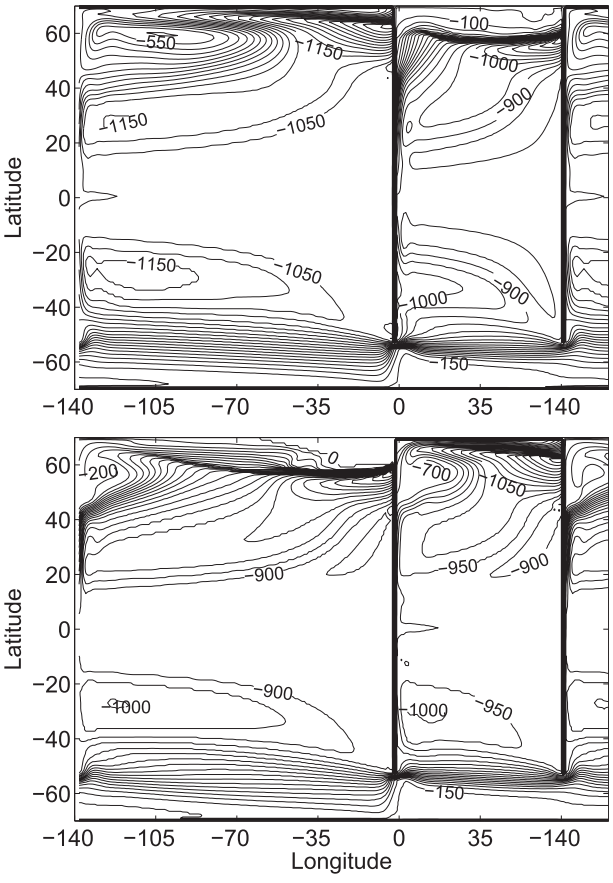

FIG. 8. Contours of the height (m) of the isopycnal b_m = 0.0076 m s^{-2} for (top) narrow-basin sinking (thick black line in Fig. 6) and (bottom) wide-basin sinking (thick black line in Fig. 7). The domain is 210° periodic: the western 20° of the wide basin is repeated to the right of the panels. Contour interval is 50 m.

circulation is quasi-adiabatic: the northward flow at intermediate depths follows isopycnals fairly well in the Southern Hemisphere, while the quasi-adiabatic residual flow in the Northern Hemisphere is augmented by a diffusively driven positive cell. The circulation has the same pattern as estimates of observed transport for upper, intermediate, and deep water (Talley et al. 2011), but the transports from the model shown here are about 30% smaller than observed transports, because the maximum wind stress in the Southern Hemisphere is about half of the value observed in nature, and the domain is only 210° wide. The deep overturning in the wide basin is characterized by two weak diffusively driven counterrotating cells each confined to a single hemisphere with maximum residual transport of about 6 Sv.

We also force a wide-sinking circulation with sinking in the wide basin and upwelling in the narrow basin. This state is achieved by decreasing the freshwater flux in the Northern Hemisphere of the wide basin by about 0.06 Sv, with a corresponding uniform increase elsewhere, until the circulation reverses (Fig. 7). Even though the active basin for wide sinking is twice as big as the active basin for narrow sinking, the amplitude of the ROC is about the same in the two cases, in agreement with the simple model described earlier. Once a new steady state is achieved, the freshwater flux can be brought back to the symmetric profile shown in Fig. 5, and eventually, in about 3000 years, the circulation reverts to sinking in the narrow basin.

In addition to the thickness-weighted average fields as a function of latitude and buoyancy, we consider the cumulative transports above a given buoyancy surface, which are a good measure of the bulk transport by the upper branch of the overturning. The bounding buoyancy surface b_m is chosen to be 0.0076 m s^{-2}: this choice captures most of the transport of the intermediate water cell while avoiding the diffusive abyssal cell (which forms only small amounts of bottom water in this model). The zonally averaged position of this surface is shown by the thick black lines in Figs. 6 and 7, and its height as a function of latitude and longitude is shown in Fig. 8 for both narrow sinking (top panel) and wide sinking (bottom panel). It is clear that the isopycnals, especially at the eastern boundary, are shallower in the active basin. This is consistent with the results of the simple model (Table 2), and with observations, which show that neutral density surfaces with maximum depths of around 1000 m are deeper in the Indo-Pacific than in the Atlantic (Fig. 1).

In the channel, the barotropic flow has a wavelike structure that is asymmetric between basins. Therefore, to illustrate the transports in the narrow and wide

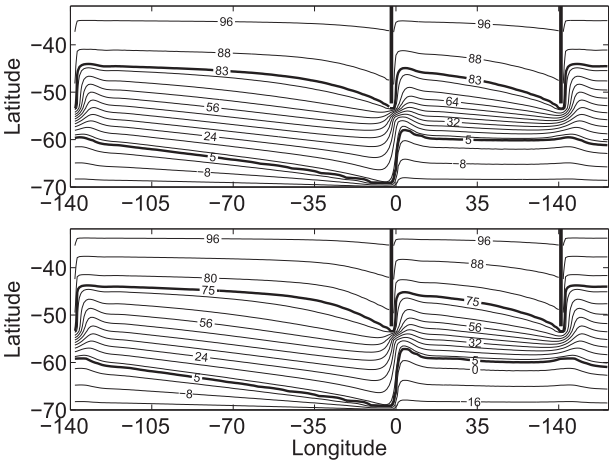

FIG. 9. Contours of the pseudostreamwise coordinate (Sv) used to evaluate the divergence of the residual velocity for (top) narrow-basin sinking and (bottom) wide-basin sinking. The contours are constructed using the barotropic streamfunction between the thick contours and tapered to latitude circles to the north and south of the displayed area. The domain is 210° periodic: the western 20° of the wide basin is repeated to the right of the figure.

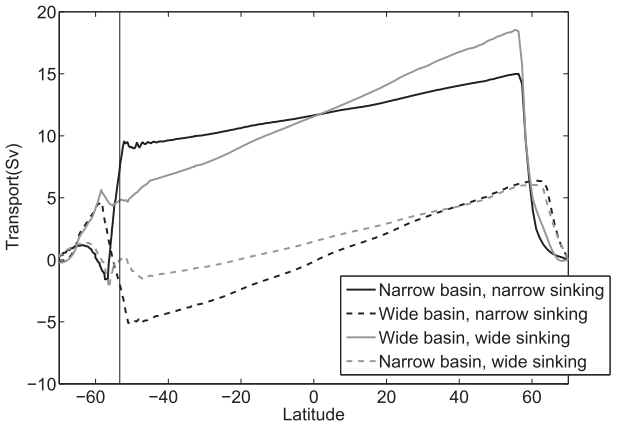

FIG. 10. The zonally average thickness-weighted meridional transports integrated above the isopycnal $b = 0.0076\,\mathrm{m\,s^{-2}}$ for narrow-basin sinking (black lines) and wide-basin sinking (gray lines). The thin vertical line denotes the northern edge of the circumpolar region.

sectors of the southern part of the domain, it is best to use a pseudostreamwise horizontal coordinate system, which follows the barotropic streamlines Ψ near the channel edge and relaxes to latitude circles both near the southern boundary of the domain and into the basin (32°S is the latitude chosen). This tapering is necessary to avoid closed contours in the streamlines of Ψ, which would make the coordinate system unusable. Contours of the pseudostreamwise coordinate system are shown in Fig. 9. This coordinate system allows us to visualize the across-stream transport in each sector by considering the divergence out of a volume bounded by an isopycnal and the surface in the vertical direction, by the southern boundary and a barotropic streamline in the meridional direction, and by the longitudes of the western and eastern boundaries of the narrow and wide sectors in the zonal direction. To calculate the across-stream transport, it is easier and numerically more accurate to integrate the horizontal divergence of the vertically integrated velocity over a surface in the latitude–longitude plane as shown in Fig. 9 and use Gauss's theorem. In order for vector calculus to be valid in this context, it is necessary to introduce a dual set of nonorthogonal unit vectors (Young 2012), such that

$$\mathbf{e}^1 = \hat{\mathbf{i}} \quad \text{and} \quad \mathbf{e}^2 = \nabla\Psi, \quad \text{and} \tag{14}$$

$$\mathbf{e}_1 = \frac{\Psi_y \hat{\mathbf{i}} - \Psi_x \hat{\mathbf{j}}}{\Psi_y} \quad \text{and} \quad \mathbf{e}_2 = \frac{\hat{\mathbf{j}}}{\Psi_y}. \tag{15}$$

The velocity divergence can then be calculated in the coordinate system most appropriate for the model's output and this gives the result:

$$\int_{A(\Psi)} \nabla\cdot\mathbf{u}\,dA = \int_{C(\Psi)} \mathbf{u}\cdot\mathbf{e}^2\,dl - \int_{-L}^{y(\Psi)} \mathbf{u}\cdot\mathbf{e}^1\,dy\bigg|_{\text{left}} + \int_{-L}^{y(\Psi)} \mathbf{u}\cdot\mathbf{e}^1\,dy\bigg|_{\text{right}}, \tag{16}$$

where $\mathbf{u} = u^1\mathbf{e}_1 + v^1\mathbf{e}_2 = u\mathbf{i} + v\mathbf{j}$. The northward transport across the barotropic streamline segment $C(\Psi)$ is balanced by the zonal transport of the east–west velocity (and not the along-stream velocity), as well as the small diapycnal velocity associated with the area-integrated horizontal divergence.

The cross-stream transport is then taken to be the first term on the rhs of (16) and is shown in Fig. 10, where the equivalent latitude is defined to span the same area enclosed by $A(\Psi)$ within each sector. North of 32°S the meridional transport is plotted instead.

The transports shown in Fig. 10 can be interpreted in the context of the simple model. There is more diffusive upwelling in the wide basin than in the narrow basin and by volume conservation $(\int\int_{-h}^{0} v\,dz\,dx)_y = \int w\,dx$, so the gradient of the lines in Fig. 10 is bigger for the wide basin than for the narrow basin. In the simple model, it is assumed that in the Northern Hemisphere of each basin, the diffusive upwelling north of the equator is balanced by buoyancy-driven sinking at the northern end of the basin. Therefore, ψ_N for the MITgcm simulations should be measured at the equator. About 12 Sv of transport crosses the equator in the active basin of both the narrow-sinking and wide-sinking states. Table 2 compares the

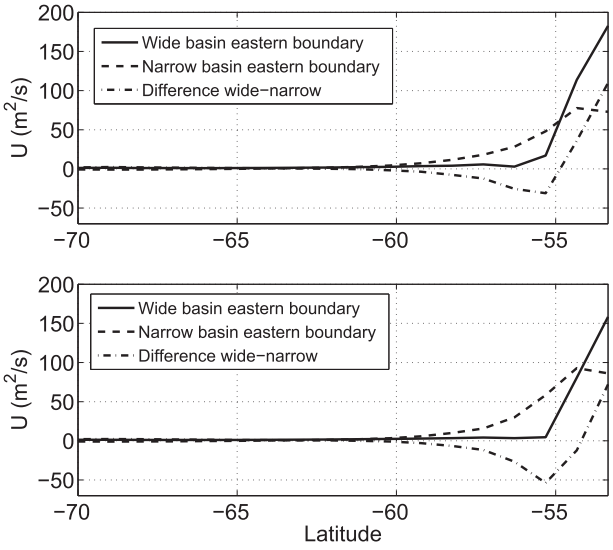

FIG. 11. Zonal transport per unit length U, integrated above the isopycnal $b = 0.0076\,\mathrm{m\,s^{-2}}$ at the eastern boundaries of the wide basin (solid line) and the narrow basin (dashed line) and their difference (dash–dotted line) for (top) narrow sinking and (bottom) wide sinking. The difference integrated across the whole channel in the Atlantic sinking case is 8.2 Sv (top) and in the Pacific sinking case it is −3.1 Sv (bottom).

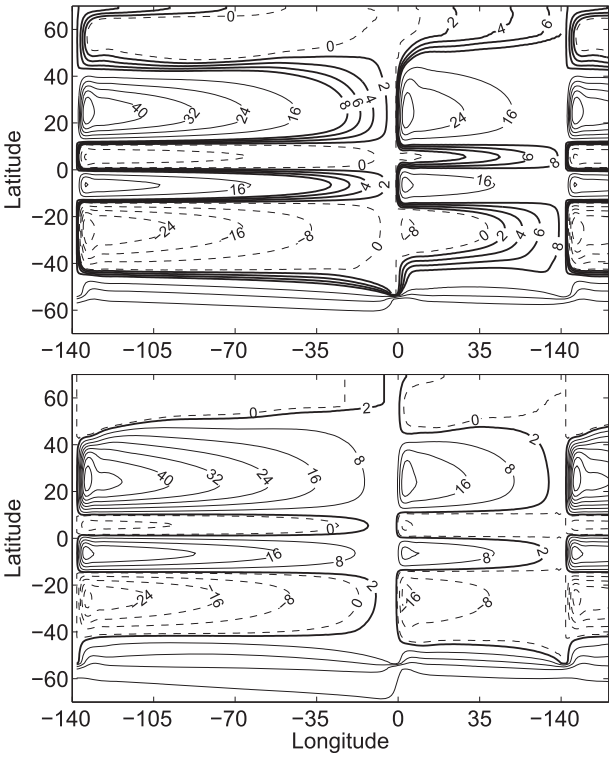

FIG. 12. Streamlines of the transport (Sv) above $b_m = 0.0076\,\mathrm{m\,s^{-2}}$ for (top) narrow-basin sinking and (bottom) wide-basin sinking. The streamlines are constructed by integrating the thickness-weighted zonal flow in latitude. The contour interval is 8 Sv for the thin lines and 2 Sv for the thick lines, which denote the interbasin exchange flow. Negative streamlines are dashed. The domain is 210° periodic: the western 20° of the wide basin is repeated to the right of the panels.

results of the numerical study to the simple model described in section 2.

South of the edge of the semienclosed basin, the pressure and buoyancy is continuous in longitude. The difference in eastern boundary isopycnal heights at the southern edge of the basins leads to an east–west height difference within each basin. This difference is associated with the geostrophically balanced meridional transport ψ_g at the northern edge of the channel, which is out of the passive basin and into the active basin. At the latitude where the continental boundaries terminate, the meridional exchange velocity turns from meridional to zonal in a narrow quasi-zonal jet connecting the two basins. The transport through 0° and 70°E/140°W is shown in Fig. 11. In both the narrow-sinking and wide-sinking states, the flow in the channel is westward, but there is a difference in transport between the eastern and western sides of the active basin because of this quasi-zonal jet. The exchange flow ψ_g causes the transport on the western side of the active basin to be larger by 8.2 Sv in the case of narrow sinking, but only 3.1 Sv in the case of wide sinking.

There are three important differences between the narrow-sinking and wide-sinking states illustrated here: 1) although the width of the wide basin is twice that of the narrow basin, the wide-sinking ROC is only slightly bigger than the narrow-sinking ROC (Fig. 10); 2) the net zonal inflow in the circumpolar region is from the wide to the narrow basin in the narrow-sinking ROC and opposite in the wide-sinking ROC (cf. the difference between the zonal transport entering at the western boundary and the flow exiting at the eastern boundary in Fig. 11); and 3) the net zonal flow exchanged between the two basins is larger for the narrow-sinking ROC. The difference in the zonal flows at the southern edges of the basins is associated with a change in the depths of isopycnals at the eastern boundaries: an example of this difference in depths is shown in Fig. 8.

5. Horizontal structure of the flow

The zonally averaged view of the upper branch of the ROC hides the rich zonal structure of the flow, which is strongly shaped by the wind-driven gyres. In Fig. 12, to visualize the horizontal distribution of the ROC, we contour the streamfunction associated with the zonal transport above the isopycnal b_m (shown by a thick line

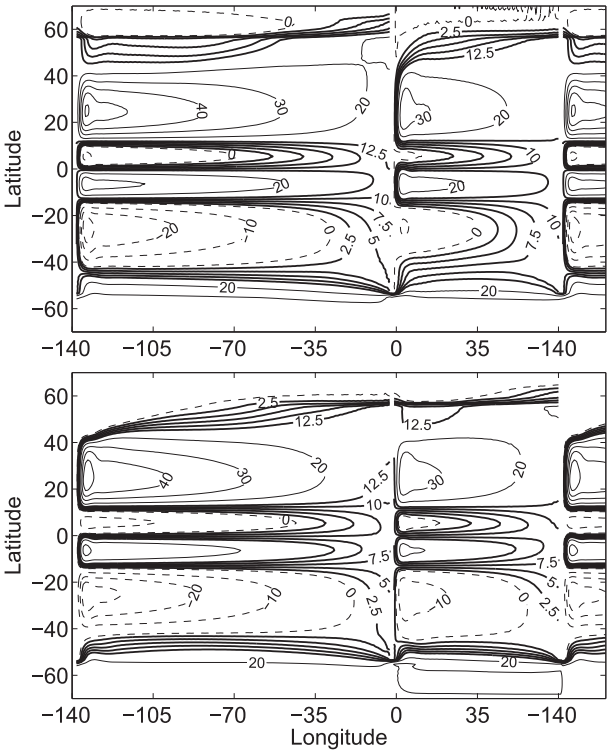

FIG. 13. Isolines of ϕ_d defined in (17) (Sv) for (top) narrow-basin sinking and (bottom) wide-basin sinking. The contour interval is 10 Sv for the thin lines and 2.5 Sv for the thick lines, which denote the interbasin exchange flow. Negative values of ϕ_d are dashed. The domain is 210° periodic: the western 20° of the wide basin is repeated to the right of the figure.

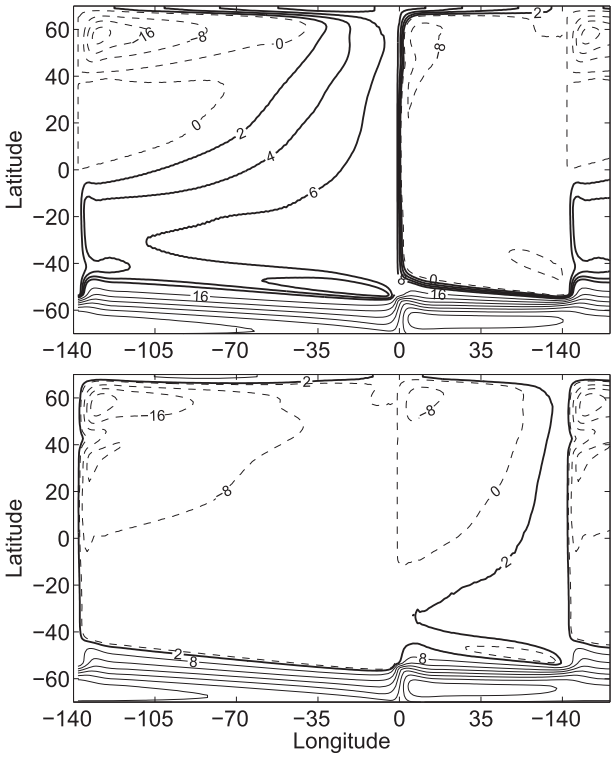

FIG. 14. Streamlines of the transport (Sv) between $b = 0.0076\ \mathrm{m\,s^{-2}}$ and the bottom for (top) narrow-basin sinking and (bottom) wide-basin sinking. The streamlines are constructed by integrating the thickness-weighted zonal flow in latitude. The contour interval is 8 Sv for the thin lines and 2 Sv for the thick lines, which denote the interbasin exchange flow. Negative streamlines are dashed.

in Figs. 6 and 7). The streamfunction is obtained by integrating the vertically integrated zonal transport northward starting from the southern boundary of the domain. The flow is horizontally divergent because of diapycnal flow in the interior and in the outcrop regions, so not all of the ROC transport is captured. This view of the ROC clearly shows the exchange flow between the two basins, highlighted by thick contours in Fig. 12. The exchange flow exits the passive basin on the western boundary, immediately turns east in a narrow zonal jet, and enters the active basin on the western boundary. From there, the wind-driven gyres induce large-scale meanders, modulating the meridional transport into alternating broad flows around the anticlockwise gyres and narrow western boundary currents to the west of clockwise gyres. Finally, the exchange flow sinks in the northeast sector of the active basin. Comparing narrow-basin sinking with wide-basin sinking, it is clear that the exchange flow is less in the latter case, but the pathways are qualitatively similar.

To visualize all of the transport, including the horizontally divergent portion, Fig. 13 shows the contours of a pseudostreamline ϕ_d constructed by adding the diapycnal contribution to the integrated zonal transport, that is

$$\phi_d = -\int_{-L}^{y} d\hat{y}\left[U(x,\hat{y}) - \int_0^x d\hat{x}\,\varpi(\hat{x},\hat{y})\right], \qquad (17)$$

where U is the zonal transport above the isopycnal b_m, and ϖ is the diapycnal velocity across the same isopycnal. This construction gives some apparent flow through the solid boundaries, but it has the advantage of illustrating the contribution of all the components of the ROC. In particular, it shows that the ROC in the active basin is primarily connected to the diffusive overturning in the Southern Hemisphere of the active basin, while the Northern Hemisphere of the passive basin does not participate in the upper branch, in accordance with the zonally averaged view of Figs. 6 and 7. In both views of the flow, the meridional throughflow velocity in the regions of anticlockwise circulation is larger for narrow-basin sinking.

To characterize the lower branch of the ROC, a streamfunction is constructed by integrating the zonal transport between b_m and the bottom. The streamlines thus obtained are shown in Fig. 14. In the active basin

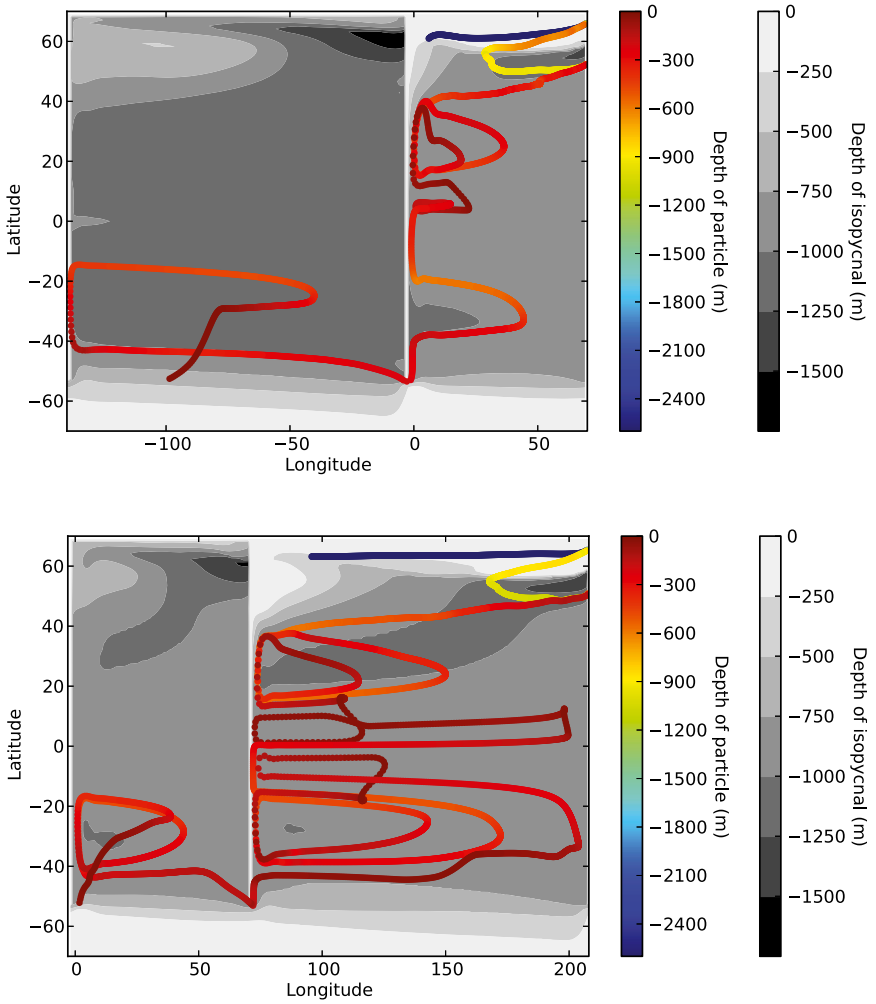

FIG. 15. The depth (m) of the isopycnal $b_m = 0.0076\,\mathrm{m\,s^{-2}}$ is plotted in grayscale for (top) narrow sinking and (bottom) wide sinking. This isopycnal divides the upper branch of the ROC from the lower branch. The location of the trajectory of a particle is shown in rainbow colors, with one point plotted every 14 days, and the color indicates particle depth (m). The active basin is plotted on the left in both cases, so that a continuous particle track is visible. The particles are initialized at the surface and at the northern edge of the channel in the passive sector. Trajectories that pass first into the passive basin and then into the active basin are chosen. The domain is 210° periodic.

the exchange flow is almost entirely confined to the western boundary, except at the southern boundary of the basin, where it turns into a quasi-zonal flow before entering the passive basin at the eastern boundary, and at the boundary between the subpolar and subtropical gyres, where excursions in the interior occur, as observed by Bower et al. (2009). The interior flow in the active basin is a mixture of the classical Stommel–Arons poleward flow, modified by the wind-driven gyres, more prominently so in the wide basin, where the wind gyres are stronger. The view of the return flow of the ROC offered by ϕ_d (not shown), defined in (17), shows that the meridional connection between the two basins does not extend to the Northern Hemisphere of the passive basin, as already seen in Figs. 6, 7, and 13.

Finally, the three-dimensional structure of the ROC can be partially visualized using particle trajectories. Figure 15 shows the paths of particles that are initialized at the surface at the northern edge of the channel in the passive sector. The particle trajectories shown are chosen to highlight the path of the Ekman transport ψ^p_{Ek} as it enters the passive basin, turns, and becomes the interbasin flow ψ_g that flows around the continental boundary and into the active basin. The particles initially move northward in the Ekman layer and are then subducted in the passive basin, getting caught in both the

tropical and subtropical gyres. The particles do not cross the equator in the passive basin, but move approximately adiabatically into the active basin. There, they go northward until they sink in the northeast part of the subpolar gyre. The transit time from entering the active basin to the sinking location is highly dependent on particle initialization: particle transit time varies with the depth of the particle and with the number of times it goes around in the gyres. In Fig. 15, the transit time from the channel to the sinking location is 125 years for the narrow sinking case and about 175 years for the wide sinking case.

6. Conclusions

In a two-basin simplified configuration of the World Ocean, with one wide and one narrow basin connected by a reentrant channel, the meridional overturning circulation prefers a state with sinking at the northern edge of the narrow basin balanced by upwelling elsewhere. The salt–advection feedback reinforces this preference. A wide-sinking circulation with sinking at the northern edge of the wide basin can be coerced by imposing reduced freshwater flux in this region, but this state is unstable to forcing that is zonally symmetric. The exchange flow between the basins is maximized in the narrow-basin sinking state, leading to a larger average depth of intermediate isopycnals in the passive versus the active basin. This difference in isopycnal depths between basins results in a higher sea surface height in the passive basin compared to the active basin.

The total residual transport is essentially fixed by the strength of the wind stress and the eddies in the ACC and by the diapycnal upwelling into the upper branch of the ROC. These quantities are approximately independent of the location of the sinking: if sinking were to occur in the North Pacific rather than the North Atlantic, the strength of the ROC transport would be about the same, even though the Indo-Pacific is much larger than the Atlantic. Consequently, the transport per unit width, or the typical meridional velocity associated with the upper (and lower) branch of the ROC, would be smaller for North Pacific sinking compared to North Atlantic sinking, unless the meridional transport is all concentrated in a narrow boundary current.

The approximate independence of the ROC transport on the sinking location implies that the throughflow velocity is faster when sinking occurs in the narrow basin. In addition, a plan view of the upper branch of the overturning circulation reveals that the northward path of the ROC "snakes" around the gyres. When passing clockwise gyres, the overturning streamlines follow the western boundary, and so the velocity on these streamlines is high and there is little time for exchange of salinity with the atmosphere. When passing anticlockwise gyres, the streamlines move to the eastern side of the gyre and the flow is slower so there is more time for exchange of salinity with the atmosphere. The complexities of the three-dimensional circulation may be important in setting the distribution of tracers, especially salinity, which strongly controls the range of surface buoyancy shared between the sinking region and the upwelling region in the circumpolar current. Maximizing this range of shared buoyancies allows efficient adiabatic transport along the isopycnals connecting the two hemispheres. Further analysis of the implications of this flow field to tracer transport is deferred to a subsequent study.

Acknowledgments. C.S.J. and P.C. are supported by the National Science Foundation under Grant OCE-1258887 and the Office of Science (BER), U.S. Department of Energy, under Grant DE-SC0005100. Computational resources were provided by XSEDE consortium, which is supported by National Science Foundation Grant ACI-1053575. Thanks go to Jinbo Wang, who contributed the particle trajectory code, and to David Marshall and Johan Nilsson for their helpful reviews.

REFERENCES

Allison, L. C., 2009: Spin-up and adjustment of the Antarctic Circumpolar Current and global pycnocline. Ph.D. thesis, University of Reading, 215 pp.

Antonov, J. I., R. A. Locarnini, T. P. Boyer, A. V. Mishonov, and H. E. Garcia, 2006: *Salinity*. Vol. 2, *World Ocean Atlas 2005*, NOAA Atlas NESDIS 62, 182 pp.

Bower, A. S., M. S. Lozier, S. F. Gary, and C. W. Boning, 2009: Interior pathways of the North Atlantic meridional overturning circulation. *Nature*, **459**, 243–247, doi:10.1038/nature07979.

Danabasoglu, G., and J. C. McWilliams, 1995: Sensitivity of the global ocean circulation to parameterizations of mesoscale tracer transports. *J. Climate*, **8**, 2967–2987, doi:10.1175/1520-0442(1995)008<2967:SOTGOC>2.0.CO;2.

Ferrari, R., S. M. Griffies, A. J. G. Nurser, and G. K. Vallis, 2010: A boundary-value problem for the parameterized mesoscale eddy transport. *Ocean Modell.*, **32**, 143–156, doi:10.1016/j.ocemod.2010.01.004.

Gent, P. R., and J. C. McWilliams, 1990: Isopycnal mixing in ocean circulation models. *J. Phys. Oceanogr.*, **20**, 150–155, doi:10.1175/1520-0485(1990)020<0150:IMIOCM>2.0.CO;2.

Gnanadesikan, A., 1999: A simple predictive model for the structure of the oceanic pycnocline. *Science*, **283**, 2077–2079, doi:10.1126/science.283.5410.2077.

Hughes, T. M. C., and A. J. Weaver, 1994: Multiple equilibria of an asymmetric two-basin ocean model. *J. Phys. Oceanogr.*, **24**, 619–637, doi:10.1175/1520-0485(1994)024<0619:MEOAAT>2.0.CO;2.

Huisman, S., H. A. Dijkstra, A. von der Heydt, and W. P. M. de Ruijter, 2009: Robustness of multiple equilibria in the global ocean circulation. *Geophys. Res. Lett.*, **36**, L01610, doi:10.1029/2008GL036322.

Locarnini, R. A., A. V. Mishonov, J. I. Antonov, T. P. Boyer, and H. E. Garcia, 2006: *Temperature*. Vol. 1, *World Ocean Atlas 2005*, NOAA Atlas NESDIS 61, 182 pp.

Marotzke, J., and J. Willebrand, 1991: Multiple equilibria of the global thermohaline circulation. *J. Phys. Oceanogr.*, **21**, 1372–1385, doi:10.1175/1520-0485(1991)021<1372:MEOTGT>2.0.CO;2.

Marshall, D. P., R. D. Munday, L. C. Allison, R. J. Hay, and H. L. Johnson, 2016: Gill's model of the Antarctic Circumpolar Current, revisited: The role of latitudinal variations in wind stress. *Ocean Modell.*, **97**, 37–51, doi:10.1016/j.ocemod.2015.11.010.

Marshall, J., A. Adcroft, C. Hill, L. Perelman, and C. Heisey, 1997a: A finite-volume, incompressible Navier Stokes model for studies of the ocean on parallel computers. *J. Geophys. Res.*, **102**, 5753–5766, doi:10.1029/96JC02775.

——, C. Hill, L. Perelman, and A. Adcroft, 1997b: Hydrostatic, quasi-hydrostatic, and nonhydrostatic ocean modeling. *J. Geophys. Res.*, **102**, 5733–5752, doi:10.1029/96JC02776.

Munk, W. H., 1966: Abyssal recipes. *Deep-Sea Res. Oceanogr. Abstr.*, **13**, 707–730, doi:10.1016/0011-7471(66)90602-4.

Nilsson, J., P. L. Langen, D. Ferreira, and J. Marshall, 2013: Ocean basin geometry and the salinification of the Atlantic Ocean. *J. Climate*, **26**, 6163–6184, doi:10.1175/JCLI-D-12-00358.1.

Prather, M. J., 1986: Numerical advection by conservation of second-order moments. *J. Geophys. Res.*, **91**, 6671–6681, doi:10.1029/JD091iD06p06671.

Redi, M. H., 1982: Oceanic isopycnal mixing by coordinate rotation. *J. Phys. Oceanogr.*, **12**, 1154–1158, doi:10.1175/1520-0485(1982)012<1154:OIMBCR>2.0.CO;2.

Reid, J. L., 1961: On the temperature, salinity, and density differences between the Atlantic and Pacific Oceans in the upper kilometre. *Deep-Sea Res.*, **7**, 265–275, doi:10.1016/0146-6313(61)90044-2.

Seidov, D., and B. J. Haupt, 2005: How to run a minimalist's global ocean conveyor. *Geophys. Res. Lett.*, **32**, L07610, doi:10.1029/2005GL022559.

Stocker, T. F., and D. G. Wright, 1991: A zonally averaged ocean model for the thermohaline circulation. Part II: Interocean circulation in the Pacific-Atlantic basin system. *J. Phys. Oceanogr.*, **21**, 1725–1739, doi:10.1175/1520-0485(1991)021<1725:AZAOMF>2.0.CO;2.

Stommel, H., and A. B. Arons, 1959: On the abyssal circulation of the world ocean—II. An idealized model of the circulation pattern and amplitude in oceanic basins. *Deep-Sea Res.*, **6**, 217–233, doi:10.1016/0146-6313(59)90075-9.

Talley, L. D., 2013: Closure of the global overturning circulation through the Indian, Pacific, and Southern Oceans: Schematics and transports. *Oceanography*, **26**, 80–97, doi:10.5670/oceanog.2013.07.

——, G. L. Pickard, W. J. Emery, and J. H. Swift, 2011: *Descriptive Physical Oceanography: An Introduction*. 6th ed., Academic Press, 560 pp.

Toggweiler, J. R., and B. Samuels, 1993: Is the magnitude of the deep outflow from the Atlantic Ocean actually governed by Southern Hemisphere winds? *The Global Carbon Cycle*, M. Heimann, Ed., NATO ASI Series, Vol. 15, Springer, 333–366, doi:10.1007/978-3-642-84608-3_13.

Wolfe, C. L., and P. Cessi, 2010: What sets the strength of the mid-depth stratification and overturning circulation in eddying ocean models? *J. Phys. Oceanogr.*, **40**, 1520–1538, doi:10.1175/2010JPO4393.1.

——, and ——, 2015: Multiple regimes and low-frequency variability in the quasi-adiabatic overturning circulation. *J. Phys. Oceanogr.*, **45**, 1690–1708, doi:10.1175/JPO-D-14-0095.1.

Young, W. R., 2012: An exact thickness-weighted average formulation of the Boussinesq equations. *J. Phys. Oceanogr.*, **42**, 692–707, doi:10.1175/JPO-D-11-0102.1.